Impact of Meshed HVDC Grid Operation and Control on the Dynamics of AC/DC Systems

Mehedi Hassan, *Student Member, IEEE,* Jahangir Hossain, *Senior Member, IEEE,* and Rakibuzzaman Shah, *Member, IEEE*

***Abstract*— The efficacy of long-distance and bulk power transmission largely depends on the efficient control and reliable operation of a multi-terminal high voltage direct current (MT-HVDC) grid, more precisely, a meshed HVDC grid. The capability of enduring the DC grid fault eventually enhances the reliability and improves the dynamic performance of the grid. This paper investigates the operation and control of an AC/MTDC system with bipolar topology incorporating the DC grid protection schemes. Based on the scale of a circuit breaker's operating time, the performance of three different protection strategies is compared and analyzed using DIgSILENT PowerFactory. Simulation results explicitly reveal that the dynamic performance of the MTDC grid significantly deteriorates with the slow functioning of the protection schemes, followed by a DC grid fault. Besides, prolonged recovery time causes a substantial loss of power infeed and affects the AC/DC grid's stability. Finally, to assess the frailty of the MTDC grid, a transient energy stability index (TESI) is proposed considering the voltage variation in the pre-state and post-state fault clearing interval. Relevant case studies are performed on the MTDC grid using an analytical approach and non-linear simulation studies to validate the effectiveness of the proposed index.**

***Index Terms*— Bipolar topology, DC fault, DC circuit breaker, multi-terminal DC (MTDC) grid, mesh topology, stability index.**

NOMENCLATURE

MMC	Modular multilevel converter.
MTDC	Multi-terminal DC.
P-G	Pole to ground.
P-P	Pole to pole.
HCB	Hybrid DC circuit breaker.
MCB	Mechanical DC circuit breaker.
FSW-ACCB	Fast DC switch with AC circuit breaker.
RoCoRV	Rate of change of reactor voltage.
$RoCoF_1$	Rate of change of frequency in grid-1.
TESI	Transient energy stability index.
TEVI	Transient energy variation index.
TPEI	Transient potential energy index.
TSI	Transient stability index.
P_{DC-MMC}	DC power in MMC station.
I_{MMC}	Converter current in MMC station.
$I_{DC-line}$	DC line current in MTDC grid.
t_F+	Instant, immediately after DC fault.
t_C+	Instant, immediately after fault clearance.
t_F-	Pre-fault instant.
t_B	Converter blocking instant.
t_D	Converter deblocking instant.
δ	Synchronous generator rotor angle with respect to reference machine.
δ_o	Pre-fault rotor angle of the generator.
δ_c	Generator rotor angle after fault clearance.
E	Transient energy of the MMC station in pre-state fault clearing period.
E'	Transient energy of the MMC station in post-state fault clearing period.

I. INTRODUCTION

THE Multi-terminal High Voltage Direct Current (MT-HVDC) system is a promising alternative for interconnecting asynchronous AC grids and harvesting power from offshore wind farms [1]. Due to the immense development of power electronics, the voltage source converter (VSC) based HVDC technology offers advantages over the classical line commutated converter to connect such systems [1]. Most of the existing VSC-HVDC links are conventional point-to-point connections. However, an MT-HVDC grid provides superior performance compared to the point-to-point HVDC link concerning the security, efficiency, and reliability of power systems [1]. The current multi-terminal (MT)-HVDC systems – often referred to as MTDC systems are simple in structure [2]. Moreover, the MTDC grids with more complex topologies i.e. meshed topologies are yet to be implemented due to several key challenges [2]. Lack of reliable dynamic control strategies with DC grid protection schemes, the inadequacy of flexible, and optimal DC grid power flow, and DC grid instability during contingencies are few of the significant concerns. Therefore, this paper primarily focuses on the research problem stated as follows: For the implementation of a reliable meshed MTDC grid embedded with a DC protection scheme, one of the major

Manuscript received XXXX; revised XXXX; accepted XXXX. Date of publication, XXXX; date of current version, XXXX.

M. Hassan is with the School of Engineering at Macquarie University, Sydney, Australia (e-mail: mehedi.hassan@hdr.mq.edu.au).

J. Hossain is with the School of Electrical and Data Engineering at the University of Technology Sydney, Sydney, Australia (e-mail: jahangir.hossian@uts.edu.au).

Rakibuzzaman Shah is with the School of Science, Engineering and Information Technology, Federation University Australia, Mt Helen, Australia (e-mail: m.shah@federation.edu.au).

Color versions of one or more of the figures in this paper are available online at http://ieeexplore.ieee.org.

Digital Object Identifier XXX/XX.XXX

impediments is the deficit of the dynamic studies with efficient control schemes and the DC grid instability issues.

In terms of MTDC controller aspects, different schemes have been reported in [3]-[5] to deal with the DC voltage control. Voltage droop and optimal operation based hierarchical control strategy is developed in [5] to advance the control performance of the MTDC grid. Incorporating the droop control strategy, the grid dynamics and stability of AC-MTDC systems are examined in [6]-[8]. However, the influence of the DC breaker was ignored in [3]-[8]. The impact of HVDC breakers on the MTDC grid stability is explored in [9] by root locus method and frequency domain analysis. The controllability and robustness of the MTDC grid are significantly affected due to the use of a large DC reactor [9]. However, the focus of [9] was to assess the DC grid steady state stability by linearization method.

The MTDC grid topology and converter configurations have significant impacts on the dynamics of AC grids [10]. The reconfigured meshed MTDC grid may affect the performance of the host AC system due to the alteration of power injections [11]. Authors in [11] have analyzed the performance of various hierarchical control of MTDC grids. However, the impact of the DC breaker was not considered in [11]. The impact of DC protection schemes in a three-terminal HVDC system on the frequency response of a naive AC system is reported in [12]. Nevertheless, the configuration of the control schemes and the issues of the operational stability are ignored in [12].

The transient (large disturbance) stability analysis in MTDC grid is proposed in [13], using the classical stability analysis concept of equal area criterion. However, the analysis in [13] is not suitable for DC breaker applications. Furthermore, several research studies have used the linearization method such as eigenvalue [14], [15] or impedance-based [16] approach to evaluate the stability problem under small-signal disturbances. Since the large disturbance is inevitable on the MTDC system, therefore, only the small-signal stability is not enough for analyzing the stability of a large MTDC system [17]. Thereby, non-linear methods of mixed potential theory [17] and Lyapunov based techniques [8] are used for large disturbance stability analysis in the MTDC grid. However, all these non-linear approaches are challenging to implement due to their operational complexity and limited applicability in a large AC/MTDC system.

The transient stability index is an alternative approach for the large disturbance stability assessment in a power system, which is a quantitative measure of the stability margin at any given operating point [18]. A good number of transient stability indices are available in the literature [18]. However, there is no straightforward index in the literature to measure the MTDC grid stability quantitatively.

Based on the literature review mentioned above, the research gaps are outlined as follows:

1) Deficiency of a comprehensive analysis of the meshed HVDC grid operating states which is particularly equipped with the DC protection schemes; and
2) Lack of a quantification index for assessing the transient stability of a DC grid.

Therefore, this paper aims to address those aforementioned gaps in existing literature. An efficient operation scheme of a meshed DC grid with appropriate DC breakers is developed and investigated in this paper. An extensive analysis of the protection strategies of complex DC systems is conducted including DC breakers for AC-DC dynamic assessment. In particular, the contributions of this work are summarized as follows:

1) Develop a taxonomy of the DC breaker for AC-DC dynamic studies and control design for a meshed MTDC system.
2) Construct a novel transient energy stability index to assess the dynamics of a meshed DC grid under several disturbances.
3) Conduct a comprehensive assessment to analyze the impact of DC grid reconfiguration and operating constraints due to DC breaker on the dynamics of an AC-DC system.

Therefore, all the research gaps (mentioned earlier), properly identified by a critical review of the existing literature, are clearly addressed in this paper, which confirms the novelty of the research work compared to the previous works.

The rest of the paper is organized as follows. The AC/MTDC system structure including the converter control configurations are given in Section II. Section III presents the fault dynamics and prerequisites of the DC grid protection schemes. The proposed transient energy stability index is derived in Section IV. Several case studies are provided in Section V to show the impact of the protection schemes on a system's dynamics and to validate the proposed index. The performance comparison of the stability indices is presented in Section VI. Finally, Section VII concludes the paper.

II. System Configuration and Control

The model of a large-scale AC/MTDC system with a coordinated control scheme is presented in this section.

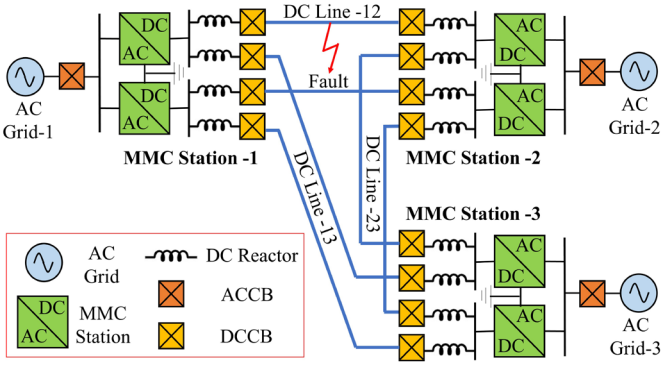

Fig. 1. Three-terminal MMC-HVDC system with bipolar topology.

A. System Description

A three-terminal bipolar MTDC grid with a meshed topology as depicted in Fig. 1 is used in this paper. The average value model of a half bridge MMC proposed in [19] is adopted here. The MTDC grid is connecting three asynchronous AC grids representing the service of cross-border power sharing.

TABLE I
PARAMETERS OF THE MTDC GRID

System Parameter	Value	System Parameter	Value
Rated AC voltage, kV	275.5	Arm inductance, mH	60
AC system Inertia, s	3.4	Arm resistance, Ω	0.006
DC voltage, kV	±500	DC cable length, km	150
Rated DC current, kA	3.4	DC cable resistance, Ω/km	0.011
Rated MMC capacity, MVA	500	DC cable inductance, mH/km	0.519
SMs per arm	200	DC cable capacitance, μF/km	0.33
SM capacitance, μF	3500	DC reactor, mH	100

In this AC/MTDC system, Grid-1 is a prevalent power system model reported in [20] with substantial modifications. Similarly, Grid-2 and Grid-3 are based on a 9-bus and two-area power system stated in [21] and [22], respectively. The order of the grid strength is Grid-1 > Grid-2 > Grid-3. All the generators of Grid-1 and Grid-3 are equipped with steam turbine governors (gov_TGOV1), automatic voltage regulators (avr_ESDC1A), and power system stabilizers (pss_STAB1). Grid-2 generators are modelled with gov_BPA GG and avr_IEEET1 type governors and exciters, respectively.

In steady state, Grid-1 draws 250 MW power from MMC-1 station by the MTDC grid. At the same time, the MTDC grid receives the power of 50 MW and 200 MW from MMC-2 and MMC-3 (by Grid-2 and Grid-3), respectively.

The bipolar MTDC grid comprises of three MMC stations rated at 500 MVA and ±500 kV. To reduce the fault current limit and realize the selective fault detection, the MTDC grid is associated with a large DC reactor of 100 mH at the end of each DC line. The system is modeled in DIgSILENT Power Factory [23]. The detailed circuit parameters of the MMC-MTDC system are given in Table I.

B. Control Structure

In the studied MTDC system, MMC-1 station operates in DC voltage and reactive power ($V_{dc}Q$) control mode. It controls the DC grid voltage to maintain the active power balance in the MTDC grid. On the other hand, MMC-2 and MMC-3 stations control their active and reactive power flow by operating in active and reactive power (PQ) control mode.

In addition, to ensure the frequency regulation in asynchronous AC grids, the MMC stations are enabled with a frequency droop supplementary controller. In MMC-1 station, a $V_{dc}f$ supplementary controller is introduced along with the DC voltage control loop. Hence, the control scheme in MMC-1 station is expressed as follows:

$$V_{DC}^{*} = V_{DC}^{o} - k_p(P^0 - P) + k_f(f - f^o) \quad (1)$$

where k_p is defined as the power droop co-efficient, k_f is the frequency droop co-efficient, V_{DC}^{*} is the reference value of DC voltage, V_{DC}^{0}, P^0 and f^0 are the set value of DC voltage, power, and frequency, respectively.

Similarly, the MMC-2 & MMC-3 are embedded with a Pf supplementary controller along with the power control loop. Therefore, the control operation is represented as follows:

$$P^{*} = P^{o} - k_v(V_{DC}^{o} - V_{DC}) + k_f'(f - f^o) \quad (2)$$

where, P^{*} is the reference value of active power, and k_v is the voltage droop coefficient defined by $k_v = 1/k_p$ [24]. Moreover, in (2), k_f' is the effective frequency droop co-efficient defined by $k_f' = k_f(1 - k_{vi}/\sum k_{vj})$, where "$i$" refers to the converter in active power control mode, while "j" is for converters in DC voltage droop mode [25]. It is to be noted that only one droop would be operated at a time for any given converter. Figure 2 illustrates the control schemes of the converter stations.

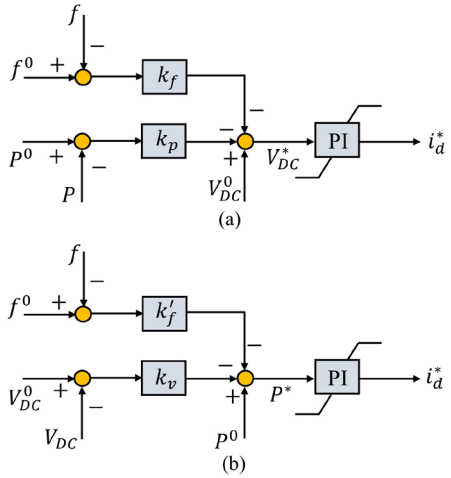

Fig. 2. Control scheme of the MTDC grid, with the supplementary controller: (a) MMC-1 station; (b) MMC-2; and MMC-3 station.

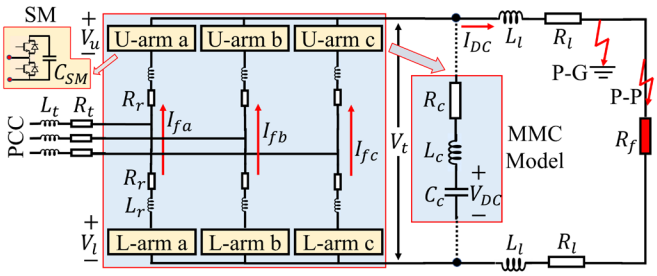

Fig. 3. Simplified equivalent circuit of an MMC-HVDC system with DC fault.

III. DC GRID CONTINGENCY

In an MTDC system, the occurrence of a DC grid fault causes the entire system to discharge through the fault within few milliseconds. Thereby, the fast interruption of fault current with a proper protection strategy is crucial to ensure a reliable MTDC system.

A typical fault event in the DC grid could be a P-G or P-P fault. Under this grid disturbance, the natural fault current rises rapidly with the following phases: (i) rising phase, (ii) transient-state phase, and (iii) steady-state phase.

After a DC fault occurrence, the discharging phenomena of the MMC-HVDC systems can be described by the equivalent circuit as shown in Fig. 3, where the MMC and DC lines are represented by a series RLC and a π-type RL model, respectively [26]. The discharging stage of the DC grid dynamics can be demonstrated by the following expression:

$$(L_c + kL_l)C_c\frac{d^2V_{DC}}{dt^2} + \left(R_c + kR_l + R_f\right)C_c\frac{dV_{DC}}{dt} + V_{DC} = 0 \quad (3)$$

where, the resistance R_c, inductance L_c and capacitance C_c of the equivalent MMC model are defined as $R_c = 2R_r/3$, $L_c = 2L_r/3$, $C_c = 6C_{SM}/N$, respectively. In (3), the integer value, $k = 1$ for a P-G fault and $k = 2$ for a P-P fault as shown in Fig. 3. Moreover, in Fig. 3, R_r and L_r are defined as the arm

resistance and inductance, respectively, R_l and L_l are denoted as the fault path resistance and inductance, respectively, R_f is the fault resistance, C_{SM} is the submodule capacitance and N is the number of submodules in each arm.

Considering a smaller value of resistance in (3), the DC current of the MMC is approximated as:

$$I_{DC} = e^{-\sigma t}\left[V_0\sqrt{\frac{C_c}{(L_c+kL_l)}}\sin(\omega t) + I_0\cos(\omega t)\right] \quad (4)$$

where, V_0 and I_0 are the pre-fault voltage and current, respectively, $\sigma = (R_c + kR_l + R_f)/2(L_c + kL_l)$ is defined as the attenuation factor and the angular frequency is denoted as $\omega = \sqrt{1/[C_c(L_c + kL_l)] - [(R_c + kR_l + R_f)/2(L_c + kL_l)]^2}$.

Due to the capacitive discharge, the DC line voltage reduces rapidly and makes the terminal voltage V_t lower than the rated voltage V_{DC}. At this stage, the rising fault current might trigger the converter protection schemes and blocks the MMC. However, the arm current cannot be switched off instantly and a free-wheeling stage exists until the arm current reaches to a zero-crossing value. Therefore, the DC grid dynamics during this period can be represented as follows:

$$V_t = V_{DC} - 2(R_r I_{fa} + L_r \frac{dI_{fa}}{dt}) \quad (5)$$

$$V_{DC} = (L_c + kL_l)\frac{dI_{DC}}{dt} + (R_c + kR_l + R_f)I_{DC} \quad (6)$$

$$I_{DC} = I_{fa} - C_c \frac{dV_{DC}}{dt} \quad (7)$$

$$I_{fa} = -\frac{C_{SM}}{N}\frac{dV_t}{dt} \quad (8)$$

where, I_{fa} is the fault current in phase-a and I_{DC} is the summation of the three phase arm currents.

After the free-wheeling period, an AC infeed stage starts to function and remains in operation until the fault current is interrupted by the circuit breaker. During this period, at least three of the arm currents remain in conduction simultaneously and might experience a commutation overlap due to overcurrent of the AC in-feed [27]. Moreover, the magnitude of the AC in-feed varies depending on different network factors (AC grid strength, transformer impedance, fault path impedance, arm reactor value etc.). Hence, the DC grid's response possess different characteristics during this period of operation and thereby, is not generalized [27], [28]. Furthermore, a faster protection scheme might break the fault current, way before the AC in-feed growing further. Finally, the DC current reaches to a new steady-state value due to the breaker operation of the protection schemes.

The DC grid protection scheme requires to maintain few steps of fault detection, location identification, isolation, and post-fault restoration to assure the grid reliability. The complete procedure of the protection strategy might suffer from communication delay and low sensitivity [29]. This can cause the fault current to reach its maximum permissible limit before the opening of the breaker. To limit the rapid growth of the fault current, DC reactor is an effective means [30]. Hence, this paper considers the rate of change of reactor voltage (RoCoRV) proposed in [30] for the accurate detection and location of the DC faults.

Two DC reactors are connected at each end of a single DC transmission line. Generally, the voltage across the DC reactors are nearly zero during the pre-fault state. Followed by a DC grid fault, the reactor voltage increases rapidly. The voltage rising rate of the DC reactors connected with the faulty line are higher than the other reactors in the healthy MTDC grid. Based on the proposed method reported in [30], the following threshold limits are considered in this paper for the fault detection:

(i) The lower and higher threshold values are 15 kV and 25 kV, respectively. The change of voltage limit (ΔV) is 10 kV.

(ii) The limit of fault detection time interval (Δt) is 375 µs.

Therefore, when the measured voltage across the DC reactor is increased from 15 kV (lower threshold) to 25 kV (higher threshold) in a time interval of higher than 375 µs, the respective DC line is treated as a faulty line and an immediate trigger signal is transmitted to the circuit breaker for isolation. It should be noted that, the primary protection scheme considered in this paper is based on the local measurements and thereby, the time-delay impact is quite negligible.

Depending on the breaking time response, three different DC breaker strategies i.e. hybrid DC circuit breaker (HCB) [31], mechanical DC circuit breaker (MCB) [32], and fast DC switch with AC circuit breaker (FSW-ACCB) [33] are considered in this paper. The HCB, MCB, and FSW-ACCB are reflected with the operating time of 5 ms, 20 ms, and 50 ms, respectively.

During the stage of breaker operation, the DC fault current can be described by the following expression [28]:

$$I'_{DC}(t) \simeq I'_0 - \frac{\alpha(V'_{DC} - V_{IV} - V_l)}{L_c + kL_l}(t - \Delta t) \quad (9)$$

where, α is the overvoltage ratio, V_{IV} is the fault-opposing inverse voltage, V_l is the line voltage and Δt is the starting time span of the breaker operation after the fault inception.

At any instant of the breaker operation, fast-acting DC breaker has a less impact on the grid dynamics, provided that all other numerator voltages in (9) is remained constant. Based on the theoretical interpretation discussed in this section, the impacts of the DC breaker operations on AC/DC system dynamics are extensively analyzed in Section V.

IV. Proposed Transient Energy Stability Index

The DC voltage dynamics of an MMC system is governed by the power balance between the AC side input and the DC side output of a VSC-station. In steady-state condition, the governing equation of the converter station can be written in per unit as follows [34]:

$$P_{AC} - P_{DC} = \frac{C_c}{S} V_{DC}\dot{V}_{DC} \quad (10)$$

where C_c and S are the equivalent capacitance and rated power of the MMC, respectively. In the transient state, any imbalance in power of the VSC-station is reflected with the variation in DC voltage. That implies,

$$\Delta P_{DC} = \Delta P_{AC} - \frac{C_c}{S}\Delta V_{DC}\Delta\dot{V}_{DC} \quad (11)$$

The change in AC power is represented by the swing equation as follows:

$$\Delta P_{AC} = \frac{2H}{f_o}\dot{\Delta f} \quad (12)$$

where, H is the inertia of the AC grid. Thereby, the change in DC power can be described as in (13).

$$\Delta P_{DC} = \frac{2H}{f_o}\dot{\Delta f} - \frac{C_c}{S}\Delta V_{DC}\Delta\dot{V}_{DC} \quad (13)$$

To facilitate the ancillary service of frequency regulation, the VSC-stations may be equipped with the coordinated control schemes as discussed in Section II. Therefore, along with the conventional droop control strategy, a supplementary controller i.e. $V_{dc}f$ or Pf is embedded in the coordinated scheme. Then, the

control operation of (1) and (2) can be explicitly represented as follows: For $V_{dc}f$ coordination,

$$\Delta V_D = -k_p \Delta P,\ \Delta V_S = k_f \Delta f \tag{14}$$

In (14), the regulation of DC voltage with droop control and supplementary control strategy is expressed by ΔV_D and ΔV_S, respectively. Similarly, for *Pf* coordination,

$$\Delta P_D = -k_v \Delta V_{DC},\ \Delta P_S = k_f' \Delta f \tag{15}$$

In (15), the regulation of active power with droop control and supplementary control is declared by ΔP_D and ΔP_S, respectively.

Henceforth, the DC power variation of (13) can be rewritten as in (16) and (17), for $V_{dc}f$ and *Pf* supplementary controllers.

$$\Delta P_{DC}^{m} = \frac{2H\Delta \dot{V}_{DC}}{k_f f_o} - \frac{C_c}{S}\Delta V_{DC}\Delta \dot{V}_{DC} \tag{16}$$

$$\Delta P_{DC}^{n} = -\frac{2Hk_v\Delta \dot{V}_{DC}}{k_f' f_o} - \frac{C_c}{S}\Delta V_{DC}\Delta \dot{V}_{DC} \tag{17}$$

In (16) and (17), ΔP_{DC}^{m} and ΔP_{DC}^{n} are the power variation of the converters equipped with $V_{dc}f$ and *Pf* controllers, respectively.

The post-fault transient energy of the system before the fault clearance is determined successively by integrating (16) and (17). In t_B~t_C time interval, the energy accumulation with the supplementary controller of $V_{dc}f$ and *Pf* are expressed by E_m and E_n, respectively (where, t_B is the converter blocking instant and t_C is the time of fault clearance). This is mathematically given by (18) and (19),

$$E_m = \int_{t_B}^{t_C} \Delta P_{DC}^{m} dt = A_m \Delta V_{DC}^{m} - B_m \Delta V_{DC}^{m\,2} \tag{18}$$

$$E_n = \int_{t_B}^{t_C} \Delta P_{DC}^{n} dt = A_n \Delta V_{DC}^{n} - B_n \Delta V_{DC}^{n\,2} \tag{19}$$

In (18) and (19), A_m, A_n, B_m, and B_n are the grid parameters defined by, $A_m = \frac{2H}{k_f f_o}$, $A_n = -\frac{2Hk_v}{k_f' f_o}$, and $B_m = B_n = \frac{C_c}{S}$.

Similarly, after the fault clearance, the transient energy E_m' and E_n' are calculated by integrating the equations of (16) and (17), respectively, within the time limit of $t_C \sim t_D$, (where, t_D is the time of converter deblocking instant). That implies,

$$E_m' = \int_{t_C}^{t_D} \Delta P_{DC}^{m}{}' dt = A_m \Delta V_{DC}^{m}{}' - B_m \Delta V_{DC}^{m\,\prime 2} \tag{20}$$

$$E_n' = \int_{t_C}^{t_D} \Delta P_{DC}^{n}{}' dt = A_n \Delta V_{DC}^{n}{}' - B_n \Delta V_{DC}^{n\,\prime 2} \tag{21}$$

Therefore, in general, the energy accumulation of an MMC-station can be presented as follows:

$$E_i = \int_{t_B}^{t_C} \Delta P_{DC}^{i} dt = A_i \Delta V_{DC}^{i} - B_i \Delta V_{DC}^{i\,2} \tag{22}$$

$$E_i' = \int_{t_C}^{t_D} \Delta P_{DC}^{i}{}' dt = A_i \Delta V_{DC}^{i}{}' - B_i \Delta V_{DC}^{i\,\prime 2} \tag{23}$$

In (22) and (23), E_i and E_i' are the accumulated transient energy of i^{th} MMC-station for pre-state ($t_B \sim t_C$) and post-state ($t_C \sim t_D$) fault clearance, respectively.

The amount of power balance in a defined transient time frame (t_B~t_D) can then be expressed by the means of a Transient Energy Variation Index (TEVI) for an MMC station as follows:

$$TEVI_{i,t} = \begin{cases} 1 - \left|\frac{E_i'}{E_i}\right|, & if\ \left|\frac{E_i'}{E_i}\right| < 1\ (acceptable) \\ 0, & if\ \left|\frac{E_i'}{E_i}\right| \geq 1\ (unacceptable) \end{cases} \tag{24}$$

Finally, the Transient Energy Stability Index (TESI) can be calculated by the following mathematical representation:

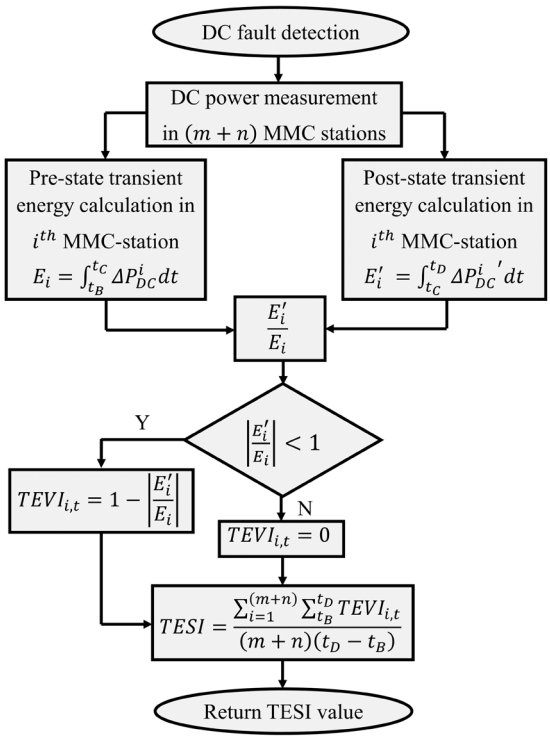

Fig. 4. Flow chart for estimating the transient energy stability index (TESI) of an MTDC grid.

$$TESI = \frac{\sum_{i=1}^{(m+n)} \sum_{t_B}^{t_D} TEVI_{i,t}}{(m+n)(t_D - t_B)} \tag{25}$$

In (25), m is the number of converter station with $V_{dc}f$, while n is the number of converter station with *Pf*. The value of TESI ranges from 0 to 1 ($0 \leq TESI \leq 1$). An MTDC grid with a lower value of the index (close to 0) specifies the system with a greater stability margin. However, the value close to 1 indicates the lower stability margin.

The entire flow chart for estimating the stability index of an MTDC grid is shown in Fig. 4. The real time implementation of the proposed method is feasible due to the availability of the local measurement devices from the primary protection and the communication channels from the back-up protection schemes. Hence, TESI is convenient to use in a practical DC system.

V. Results and Discussions

The impact of various protection schemes on the dynamics of the AC/DC system, stability analysis and the validation of the proposed index are given in this section.

A. DC Fault Clearing Performance

Two DC faults, P-G and P-P, are simulated sequentially with three different protection strategies (i.e. HCB, MCB and FSW-ACCB). For the P-G fault event, a permanent pole (positive) to ground DC fault is incepted at 0.5 s in the middle of the line connecting the stations of MMC-1 and MMC-2. On the other hand, to create the P-P fault event, a permanent pole (positive) to pole (negative) fault is applied in the same location of the line at 0.5 s.

TABLE II
SEQUENCE OF PROTECTION EVENTS FOR DC FAULT

Breaker	Events	Time Instant (s)
HCB	P-G fault inception	0.5000
	Blocking of MMC 1, 2 and 3	0.5015, 0.5020 and 0.5030
	Opening of HCB 1 and 2	0.5075
	Deblocking of MMC 2, 3 and 1	0.5093, 0.5093 and 0.5300
MCB	P-G fault inception	0.5000
	Blocking of MMC 1, 2 and 3	0.5015, 0.5020 and 0.5030
	Opening of MCB 1 and 2	0.5225
	Deblocking of MMC 2, 3 and 1	0.5305, 0.5305 and 0.5395
FSW-ACCB	P-G fault inception	0.5000
	Blocking of MMC 1, 2 and 3	0.5015, 0.5020 and 0.5030
	Opening of ACCB 1, 2 and 3	0.5525
	Opening of FSW 1 and 2	0.5565
	Closing of ACCB 1, 2 and 3	0.6725
	Deblocking of MMC 2, 3 and 1	0.6925, 0.6925 and 0.6975

The sequence of all the protection events for P-G and P-P faults are summarized in Table II. For symmetry reasons, only positive P-G fault is shown here.

The higher rising rate of the DC fault current enables the overcurrent protection scheme of the converters as soon as the arm fault current reaches to its maximum permissible limit, (2 p.u). Henceforth, to protect the arm components, the converter stations of MMC-1, MMC-2, and MMC-3 are blocked at 0.5015 s, 0.502 s, and 0.503 s, respectively. Meanwhile, the selective fault detection scheme takes time of 2.5 ms to respond the fault inception and the circuit breaker tripping signal is received at 0.5025 s. The performances of the breakers are discussed below. Due to similar characteristic response in P-P fault, only the simulation curves for P-G fault are shown here.

1) Impact of HCB operation: After receiving the tripping signal from the controller, the HCB opens at 0.5075 s. Figure 5 shows the respective transient response of the AC/MTDC system for the P-G fault. During the fault clearing process, the DC grid voltage of the healthy lines are decreased to 265 kV with a breaking current of 8.2 kA in the faulty line. All the converters are deblocked after the fault clearance. The grid power is restored to its normal operation within 230 ms after the DC fault. Moreover, the host AC system experienced unwanted rotor angle fluctuations.

2) Impact of MCB operation: The operating time of the MCB is 20 ms. Hence, after receiving the tripping signal succeeded by a DC fault, the MCB trips the breaker at 0.5225 s. Figure 6 shows the respective transient response of the AC/MTDC system for the P-G fault. The healthy grid voltage reduces up to 30 kV before clearing the fault. The breaking current of MCB is found to be of 5.1 kA for the DC fault. After the fault clearance, the converter stations of MMC-2, MMC-3, and MMC-1 are deblocked at 0.5305 s, 0.5305 s, and 0.5395 s, respectively. Finally, for a P-G fault, the DC grid retains back to its pre-fault operation with a recovery time of 580 ms. Moreover, the rotor angle deviation is settled down quickly with the fault clearance and does not affect the stability of the system.

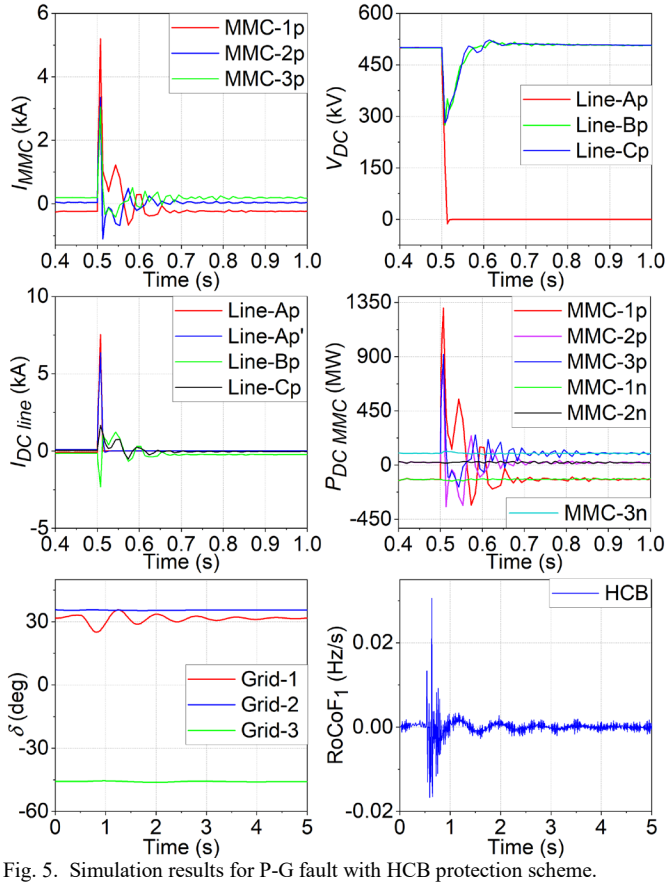

Fig. 5. Simulation results for P-G fault with HCB protection scheme.

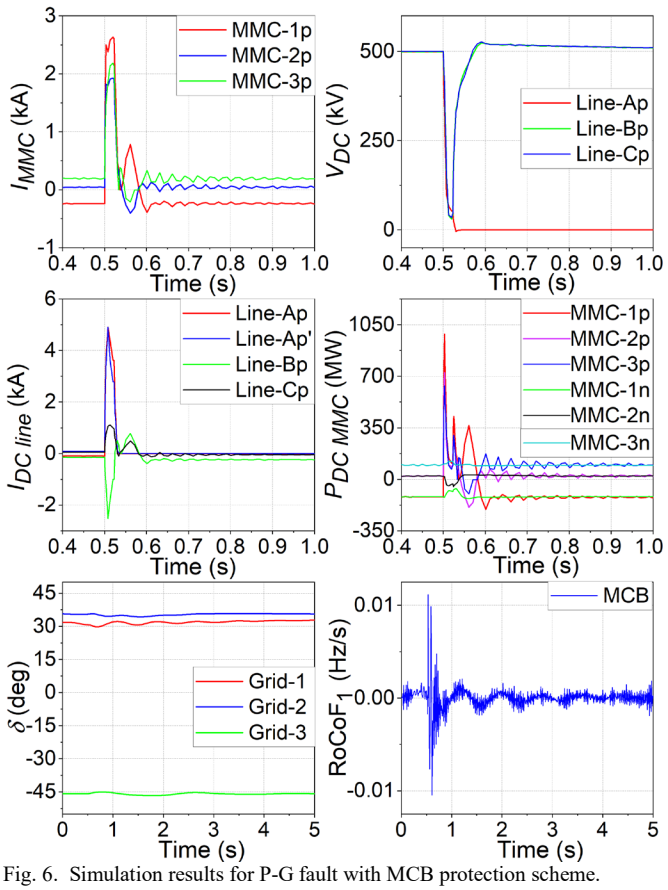

Fig. 6. Simulation results for P-G fault with MCB protection scheme.

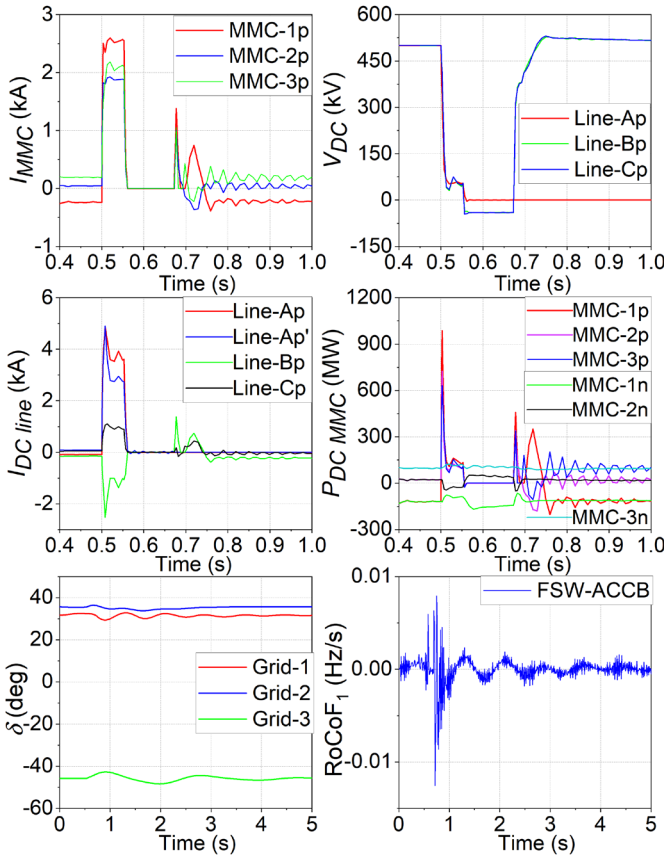

Fig. 7. Simulation results for P-G fault with FSW-ACCB protection scheme.

3) Impact of FSW-ACCB operation: Figure 7 shows the respective transient responses of the AC/MTDC system for a P-G fault with a protection scheme of FSW-ACCB. The post-fault triggering signal instructs the ACCB to operate and clear the DC fault. Considering the operating time of 50 ms, the ACCB trips at 0.5525 s to limit the fault current feeding from the AC side. The breaking currents are 4.95 kA. The fast-acting DC switch of the faulty line is opened at 0.5565 s when the DC grid is fully discharged. Considering the deionization time of 120 ms, the ACCB is then closed at 0.6725 s. To restore the DC grid, the converter stations of MMC-2, MMC-3, and MMC-1 are deblocked sequentially at 0.6925 s, 0.6925 s and 0.6975 s. Within 750 ms after the P-G fault inception, the DC grid is fully restored to continue the pre-fault operation. On the other hand, grid-1 is suffered with considerable oscillations compared to other AC generators. The oscillation is settled at 3 s after the fault clearance. However, it is worth noting that the MTDC grid with FSW-ACCB protection strategy can suffer a discontinuity of service for a DC grid fault.

4) Performance comparison: The main objective of this part is to compare the performance of an MTDC grid with different types of DC breakers. Immediately after the DC fault inception, maximum overshoot of the active power is experienced by MMC-1 for HCB protection. It is due to the fact that the HCB is operating in the rising state phase of the fault current response. In this phase, the maximum fault current of 5 kA is rapidly raised to 8.2 kA by the AC infeed current due to the blocking of converter stations. Hence, the breaking current of HCB is 8.2 kA.

On the other hand, the tripping action of the MCB and ACCB is placed in the steady-state phase of the fault current response. Therefore, their breaking currents are almost similar. In terms of the grid voltage scenarios with HCB and MCB operation, the DC voltage quickly recovers back to its pre-fault value without affecting much of the grid stability.

On the contrary, in FSW-ACCB protection strategy, due to the de-energization process of the MTDC grid, the DC voltage reduces to zero and the continuous power flow is disrupted for a long period of time. This might cause the stability problem in an AC/MTDC grid. Compared to other protection strategies, higher RoCoF and higher rotor angle deviation for a longer period is observed in the AC grid-1 for the DC grid disturbance with the FSW-ACCB strategy. Thereby, to ensure a reliable

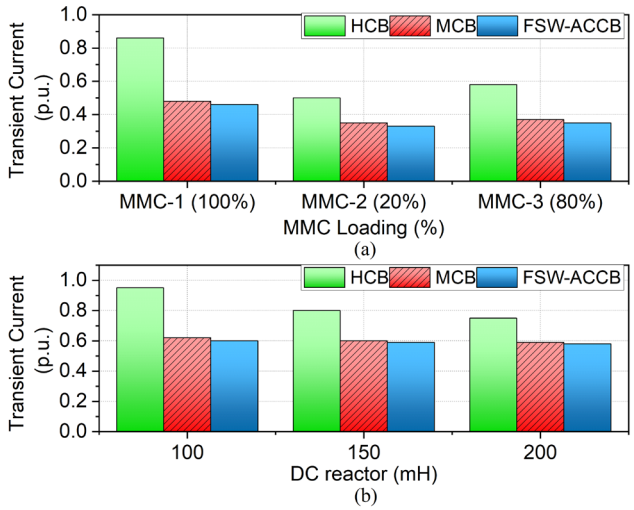

Fig. 8. Transient current responses of different protection schemes: (a) Loading conditions; (b) Different DC reactors.

operation in an AC/MTDC grid, the protection with FSW-ACCB strategy is inappropriate to implement.

5) Impact on grid dynamics: To assess the impact of the protection schemes on the AC-DC grid dynamics, the performances of the breakers are analyzed in this subsection for the following operating states:

1. MMC loading: The pre-fault loading condition of an MMC significantly influences the transient state power flow and causes the fluctuation of maximum peak current, followed by a DC grid fault. However, the converter loading level does not affect the steady-state operation of an MTDC grid.

In terms of selective protection strategies, the impact of the loading level increases with the decrease of DC breaker operating time. Hence, the operation of an HCB is mostly affected with a higher loading and lower breaking time duration as shown in Fig. 8(a).

2. MTDC grid reconfiguration: Followed by a permanent DC grid fault, an MTDC grid is reconfigured with the isolation of the DC lines using a DC grid protection strategy. The power alteration caused by the grid reconfiguration is affected considerably by the operating time duration of the circuit breaker. Hence, slow functioning breaker affects the DC grid

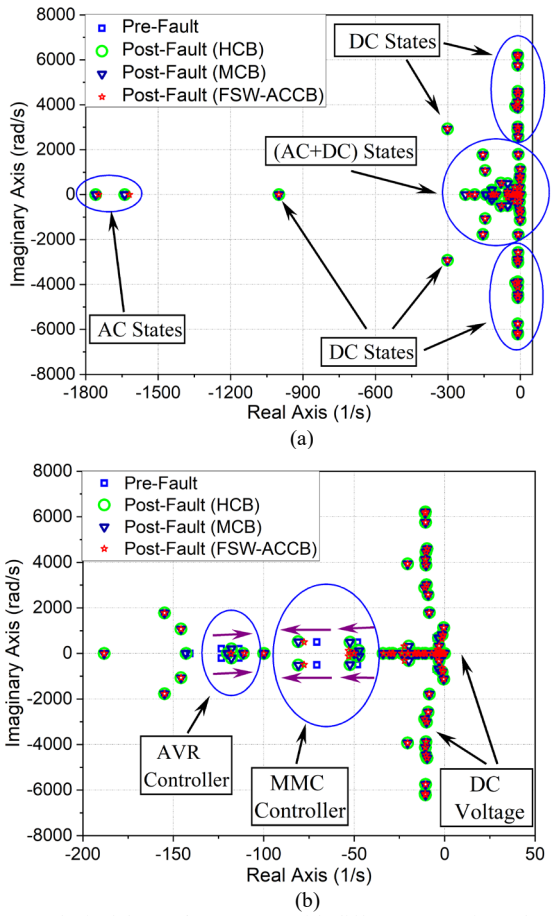

Fig. 9. Root loci of the AC/DC system with different protection schemes: (a) Compact view; (b) Enlarged view.

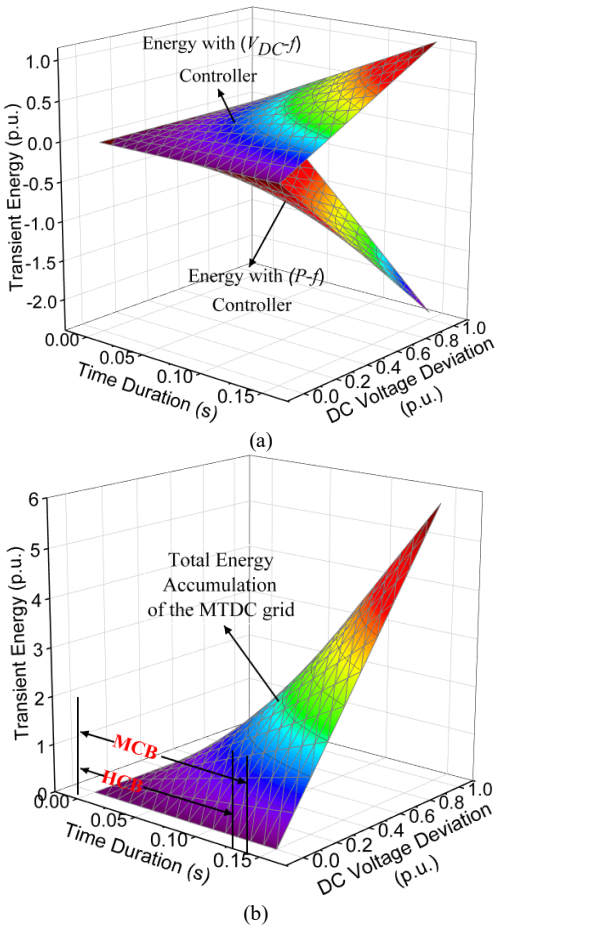

Fig. 10. Post-fault transient energy accumulation: (a) MTDC grid with $V_{dc}f$ and Pf supplementary controller (separate); (b) MTDC grid with $V_{dc}f$ and Pf supplementary controller (altogether).

most. However, the impact can be significantly reduced by increasing the value of the DC reactor as shown in Fig. 8(b).

In a nutshell, for a particular value of the DC reactor, the dynamic behavior of the AC-DC system introduces a notable impact with a larger value of the operating time. The DC power curves, rotor angle deviations, and RoCoF's shown in Figs. 5 to 7 justify the statement correctly.

B. Modal Analysis

The modal/eigenvalue analysis is carried out to evaluate the impact of different protection schemes on the dynamics of the AC/DC system.

The linearized model of the AC/DC system is represented by the state-space equation as follows:

$$\Delta \dot{\boldsymbol{x}} = \boldsymbol{A}\Delta\boldsymbol{x} + \boldsymbol{B}\Delta\boldsymbol{u} \tag{26}$$

where, $\Delta\boldsymbol{x}$ is defined as the state vector, $\Delta\boldsymbol{u}$ is the input vector, $\boldsymbol{A}$ is the state matrix and $\boldsymbol{B}$ is the input matrix of the system.

Based on the state-space equation expressed in (26), the modal analysis is performed using the Modal/Eigenvalue Analysis toolbox in DIgSILENT Powerfatory [23]. The dimension of the state matrix is 297. The eigenvalues of $\boldsymbol{A}$, respective eigen vectors and participation factors of different oscillatory modes are computed. Starting from the pre-fault base case, the eigenvalues of the state matrix are plotted with various protection strategies and respective root loci are displayed in Fig. 9.

It is found from Fig. 9 that all the eigenvalues are placed in the negative real parts which demonstrate a stable operating state. Figure 9(a) illustrates that the modes associated with the DC side states (DC Voltage, MMC Controller) are mostly dominant towards the right on left half s-plane. The enlarged view of the critical modes as shown in Fig. 9(b) reveals that the polar movements for different protection schemes are almost negligible except few states of the MMC controller and the synchronous generator's Automatic Voltage Regulator (AVR) controller.

Apart from the linear modal analysis, nonlinear simulation is also widely used in the literature to analyze the dynamic performance and stability of power systems including DC grid. However, sometimes the computational cost can be higher for a large system. An alternative approach could be the use of an appropriate stability index which is analyzed and validated in the next subsection.

C. Validation of TESI

The same MTDC system given in Fig. 1 is used as a test system to further analyze the index. It is worth mentioning that the HCB and MCB protection scheme have been used to assess the performance of the proposed index.

As mentioned earlier, the MMC-1 station is operating in $V_{dc}Q$ control mode including a $V_{dc}f$ supplementary controller. Hence, succeeded by a DC fault, the transient time power balance of the MMC-1 station will follow the relation expressed in (16).

Eventually, the energy accumulations during the pre-state and post-state fault clearance are calculated according to (18) and (20), respectively.

On the other hand, *PQ* mode and *Pf* supplementary controller are used in MMC -2 and -3. Therefore, both the stations will maintain the same power balance equation represented in (17). As a result, during the pre-state and post-state fault clearing time, the transient energy accumulation for both the stations are computed by the relation expressed in (19) and (21), respectively. The grid parameters are found to be of 7.68, 15.36, and 0.21, respectively (in p.u).

To analyze the transient state, two different case studies have been executed in the test system by introducing the DC grid faults (e.g. P-G and P-P fault). They are as follows:

i. Case I: DC fault for 125 ms (HCB) with converter deblocking time of 12 ms and 20 ms after fault clearance.
ii. Case II: DC fault for 140 ms (MCB) with converter deblocking time of 8 ms and 20 ms after fault clearance.

After the fault inception at 0.5 s, the protection scheme of HCB and MCB takes 125 ms and 140 ms, respectively to clear the fault including 120 ms of deionization time for the faulty line. The post-disturbance accumulated energy in the transient state is illustrated in Fig. 10.

1) Case I: Following a P-G temporary fault at 0.5 s, the stations of MMC-1, MMC-2, and MMC-3 are blocked at t_B= 0.501 s, 0.504 s, and 0.503 s, respectively. Considering the deionization time of the faulty line, the HCB then clears the fault at t_C = 0.6275 s. The transient state energy accumulation in this pre-state fault clearing interval is found to be of E_1= 0.98, E_2= 0.41, and E_3= 0.71 for MMC-1, MMC-2, and MMC-3, respectively (in p.u).

In the next step, all the converter stations are deblocked at t_D= 0.639 s after fault clearance and the transient state energy accumulation in this post-state fault clearing interval is E_1'= 0.29, E_2'= 0.20, and E_3'= 0.15 for MMC-1, MMC-2, and MMC-3, respectively (in p.u). Thereby, TEVI and TESI can be estimated as follows:

$$TEVI_1{}' = 1 - \left|\frac{E_1'}{E_1}\right| = 0.70,\ TEVI_2{}' = 1 - \left|\frac{E_2'}{E_2}\right| = 0.51 \text{ and}$$
$$TEVI_3{}' = 1 - \left|\frac{E_3'}{E_3}\right| = 0.79 \quad (27)$$

$$TESI' = \frac{\sum_{i=1}^{3}\sum_{t_B}^{t_D} TEVI_i{}'}{3(t_D - t_B)} = 0.66 \quad (28)$$

From (28), it is seen that $TESI'$ value is much closure to 1, which indicates lower stability margin for the DC grid system.

Similarly, for the same fault duration and blocking stage, the transient energy variation of the converter stations is re-examined with an increased deblocking time interval of 20 ms. Hence, after clearing the fault at t_C=0.6275 s, all the converter stations are deblocked at t_D=0.6475 s. The transient energy accumulation in the post-state fault clearing interval is E_1''= 0.76, E_2''= 0.61, and E_3''= 0.62 for MMC-1, MMC-2, and MMC-3, respectively (in p.u). The transient energy in the pre-state fault clearing interval will remain unchanged.

Therefore, TEVI and TESI of the converter stations are calculated by the following expressions:

$$TEVI_1{}'' = 1 - \left|\frac{E_1''}{E_1}\right| = 0.22,\ TEVI_2{}'' = 1 - \left|\frac{E_2''}{E_2}\right| = 0 \text{ and}$$
$$TEVI_3{}'' = 1 - \left|\frac{E_3''}{E_3}\right| = 0.13 \quad (29)$$

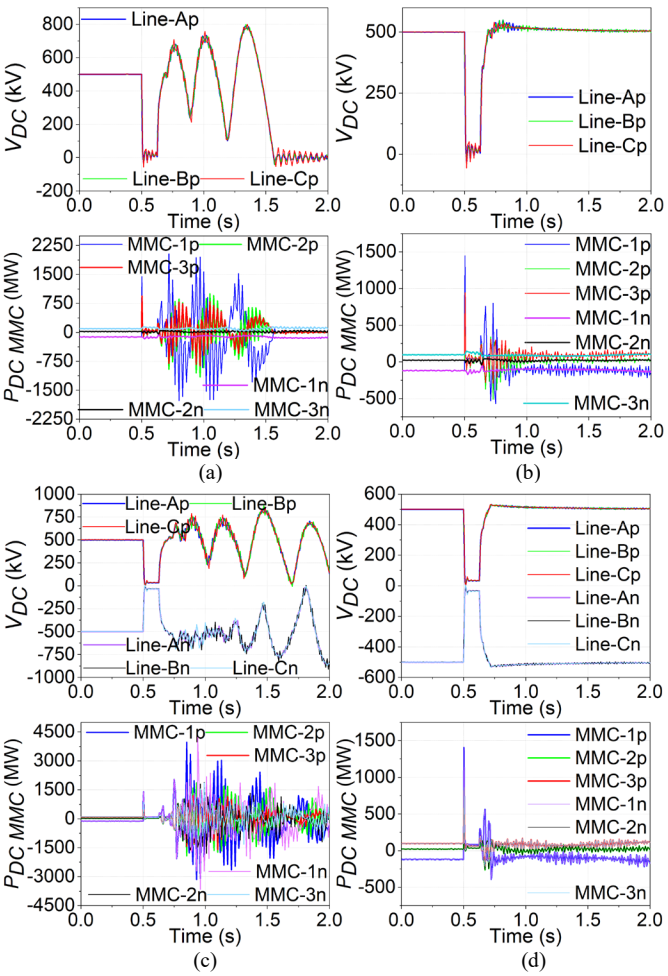

Fig. 11. Case I - DC fault transient responses with HCB: (a) P-G fault (low); (b) P-G fault (high); (c) P-P fault (low); (d) P-P fault (high).

TABLE III
TRANSIENT ENERGY STABILITY INDEX (CASE I)

Fault type	De-blocking time (ms)	TEVI of MMC 1	2	3	TESI	Comments on stability margin
P-G	12	0.70	0.51	0.79	0.66	Low
	20	0.22	0.00	0.13	0.12	High
P-P	12	0.58	0.00	0.63	0.40	Low
	20	0.38	0.00	0.31	0.22	High

$$TESI'' = \frac{\sum_{i=1}^{3}\sum_{t_B}^{t_D} TEVI_i{}''}{3(t_D - t_B)} = 0.12 \quad (30)$$

From (30), it is observed that the $TESI''$ value is much closure to 0, which indicates a higher stability margin for the DC grid.

The same analysis can be carried out for a P-P fault. To avoid the repetition, all the results of the case study are summarized in Table III. The simulation results supporting the transient energy stability index are illustrated in Fig. 11 to validate the proposed TESI.

2) Case II: Following a P-P temporary fault at 0.5 s, the stations of MMC-1, MMC-2, and MMC-3 are blocked at t_B= 0.501 s, 0.504 s, and 0.503 s, respectively. Considering the deionization time of the faulty line, the MCB then cleared the fault at t_C= 0.6425 s. Therefore, the transient state energy

accumulation in this pre-state fault clearing interval is found to be of E_1=0.98, E_2= 0.33, and E_3= 0.73 for MMC-1, MMC-2, and MMC-3, respectively (in p.u).

In the next step, all the converter stations are deblocked at t_D= 0.6507s after the fault clearance and the transient state energy accumulations in post-state fault clearing interval are E_1'= 0.29, E_2'= 0.24, and E_3'= 0.18 for MMC-1, MMC-2, and MMC-3, respectively (in p.u). For three MMC stations, TEVI and TESI can be determined as follows:

$$TEVI_1{}' = 1 - \left|\frac{E_1'}{E_1}\right| = 0.70,\ TEVI_2{}' = 1 - \left|\frac{E_2'}{E_2}\right| = 0.27 \text{ and}$$

$$TEVI_3{}' = 1 - \left|\frac{E_3'}{E_3}\right| = 0.75 \quad (31)$$

$$TESI' = \frac{\sum_{i=1}^{3}\sum_{t_B}^{t_D} TEVI_i{}'}{3(t_D - t_B)} = 0.59 \quad (32)$$

From (32), it is seen that the $TESI'$ value is far from the lower limit of 0 (zero), which indicates the lower stability margin.

Similarly, for the same fault duration and blocking stage, transient energy variation of the MMC stations is re-examined with an increased deblocking time interval of 20 ms. Hence, after clearing the fault at t_C = 0.6425 s, all the MMC stations are deblocked at t_D= 0.6625 s. The transient energy accumulations in the post-state fault clearing interval are E_1''= 0.63, E_2''= 0.55, and E_3''= 0.53 for MMC-1, MMC-2, and MMC-3, respectively (in p.u). However, the transient energy in the pre-state fault clearing interval will remain unchanged.

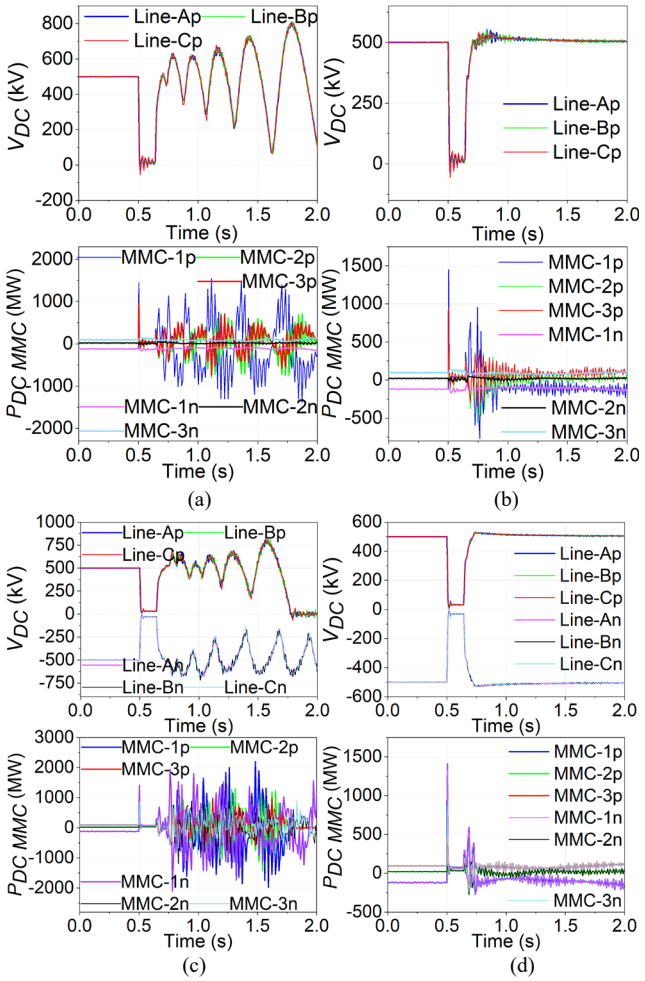

Fig. 12. Case II - DC fault transient responses with MCB: (a) P-G fault (low); (b) P-G fault (high); (c) P-P fault (low); (d) P-P fault (high).

TABLE IV
TRANSIENT ENERGY STABILITY INDEX (CASE II)

Fault type	De-blocking time (ms)	TEVI of MMC 1	2	3	TESI	Comments on stability margin
P-G	08	0.61	0.00	0.65	0.42	Low
	20	0.25	0.00	0.11	0.11	High
P-P	08	0.70	0.27	0.75	0.59	Low
	20	0.36	0.00	0.27	0.23	High

Therefore, TEVI and TESI of the converter stations are calculated as follows:

$$TEVI_1{}'' = 1 - \left|\frac{E_1''}{E_1}\right| = 0.36,\ TEVI_2{}'' = 1 - \left|\frac{E_2''}{E_2}\right| = 0 \text{ and}$$

$$TEVI_3{}'' = 1 - \left|\frac{E_3''}{E_3}\right| = 0.27 \quad (33)$$

$$TESI'' = \frac{\sum_{i=1}^{3}\sum_{t_B}^{t_D} TEVI_i{}''}{3(t_D - t_B)} = 0.28 \quad (34)$$

From (34), it is seen that the $TESI''$ value is much closure to 0, which indicates the higher stability margin (stable system).

The same analysis can be carried out for the P-G fault. To avoid repetition, all the results of the case study is summarized in Table IV. The simulation results supporting the transient energy stability index are illustrated in Fig. 12 to validate the proposed TESI.

From the results given in Table III and IV, it is evident that the types of DC breakers used in the DC system do not have a significant impact on the large disturbance DC grid stability. The deblocking of the converter is a significant contributor to the large disturbance DC grid stability. From the numerical simulation results, it is also observed that the system experienced higher oscillations under delayed deblocking, reflects higher TESI, lower stability margin.

VI. REVIEW AND COMPARISON OF STABILITY INDICES

The following section briefly reviews two well-established transient stability indices and compares their performances with the proposed TESI method.

- The Transient Stability Index (TSI) is a popular tool to determine the stability status of a power system, where all the generators are connected synchronously. The expression of TSI is defined as [18]:

$$TSI = \frac{360 - \delta_{max}}{360 + \delta_{max}} \times 100 \quad (35)$$

where, δ_{max} refers to the maximum rotor angle difference between any two generators at the same instance immediately after the fault inception. The larger value of TSI indicates a more stable system.

- The Transient Potential Energy Index (TPEI) is a generator specific index that relies on the maximum rotor angle deviation of a generator and is defined as [23]:

$$TPEI = \sum_{i=1} P_{m_i}(\delta_{0_i} - \delta_{c_i}) \quad (36)$$

where, P_{m_i} is the pre-fault mechanical power and $(\delta_{0_i} - \delta_{c_i})$ is the rotor angle deviation of i^{th} generator during the fault clearing interval. The highest TPEI value exhibits the most unstable generator of the system.

In comparison with the above-mentioned stability indices (TSI and TPEI), the proposed method (TESI) is a system

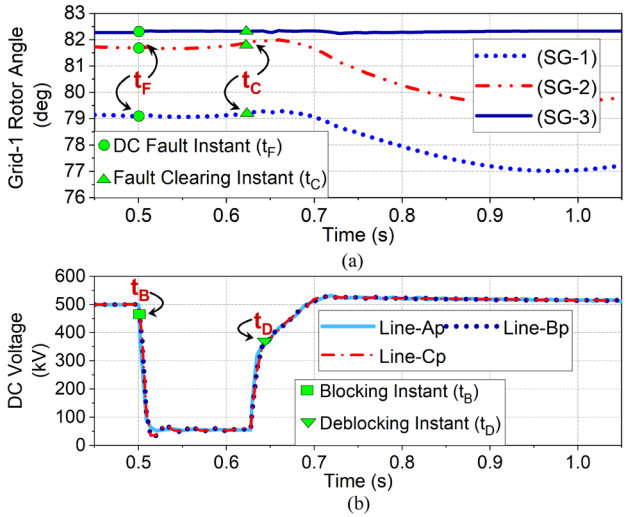

Fig. 13. DC fault (P-G) transient responses with HCB protection: (a) Grid-1 rotor angle (slow dynamics); (b) DC grid voltage (fast dynamics).

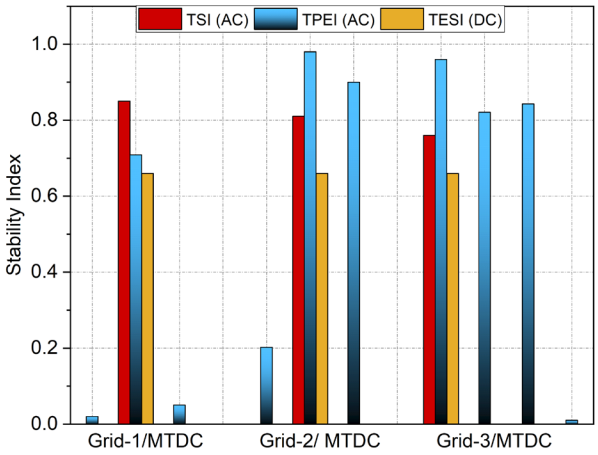

Fig. 14. Stability indices comparison for a large disturbance DC grid fault

specific stability index which quantitatively measures the stability of a DC grid. Hence, TESI works for faster system dynamics compared to TSI and TPEI. Moreover, TSI and TPEI mostly rely on rotor angle fluctuations of the system generators and therefore best suited for AC grid fault analysis. On the contrary, TESI depends on the DC voltage fluctuations which mostly fitting to DC grid fault analysis. However, in an AC/DC system, the DC grid fault affects both on the AC (rotor angle) and DC (DC voltage) side; as previously discussed in Section V. Hence, this paper compares the performance of the indices (TSI, TPEI and TESI) focusing solely on the DC side fault.

Followed by a DC grid fault on the test system as shown in Fig. 1, the slower fluctuations of rotor angles in a synchronously connected AC grid generators (for example, three synchronous generators (SG's) in Grid-1) and the faster deviations of DC grid voltages are shown in Fig. 13. The value of TSI and TPEI are calculated using the rotor angle fluctuations measured immediately after t_F and t_C respectively from Fig. 13(a). Similarly, from Fig. 13(b) the TESI value is computed measuring the DC voltage deviations at t_B and t_D instant. The comparison of the stability indices is depicted with the bar charts and tabular form as shown in Fig. 14 and Table V respectively.

TABLE V
COMPARISON OF STABILITY INDICES

Stability Index	Key Parameter	Time Frame	Stability Level	Grid	Range
TSI	Rotor angle	(t_F+)	System Level	AC (syn)	(0 ~ 100)
TPEI	Rotor angle	(t_F-) to (t_C+)	Generator Level	AC (syn)	-
TESI	DC voltage	t_B to t_D	System Level	DC	(0 ~ 1)

The TSI value shows the overall system's stability of three individual AC grids which are connected asynchronously through an MTDC grid. In response to the DC grid disturbance, AC Grid-3 is more vulnerable compared to other two AC grids as shown in Fig. 14. However, the TSI value is not capable of providing any information relating to the DC grid stability.

Rather than focusing on the system level stability, the TPEI value particularly concentrates on the stability of individual generators synchronously operating in the system. Hence, this method has no boundary limit for instability. Figure 14 illustrates that three synchronous generators in AC Grid-3 deviates largely and least deviation is observed in AC Grid-1. Therefore, within the time frame of TPEI measurement, it is not possible to assess the whole DC grid stability scenario.

Similar to the system-oriented stability analysis of TSI method, the proposed TESI method also shows a system level stability analysis, which is applicable only for DC grid. It is evident from Fig. 14 that a TESI value of 0.66 is constant in the entire MTDC grid for a particular deblocking instant, which is not possible with TSI and TPEI methods. Following a DC fault in an AC/DC system, only the TESI value is capable of rendering the response of the DC grid stability with a fixed index value. Moreover, each converter station is supposed to compute their own transient energy variation index (TEVI), which helps to identify the vulnerable converter in the MTDC grid.

VII. CONCLUSIONS

This paper investigates the impact of DC grid protection schemes on the dynamic performance of an AC/MTDC system and proposed a transient energy stability index (TESI) to quantify the DC grid stability. Three different circuit breaker strategies are adopted here with an insertion of large DC reactor. Simulation results reveal that during the transient state followed by a DC grid fault, slow functioning DC breaker severely affects the DC grid voltage and current. A converter with highest loading level experiences the maximum fluctuation of the fault current and significantly affects the transient state power flow of an MTDC grid. The impact of the loading level increases with a decrease of the DC breaker operating time. Moreover, the power degradation caused by the reconfiguration of an MTDC grid increases considerably with a larger breaking time, which can be greatly reduced by increasing the value of the DC reactor. The vulnerability state of the MTDC grid is also analyzed using the proposed index, both numerically and analytically. It is exposed that the deblocking instant of the converter significantly affects the

large disturbance DC grid stability.

In summary, the main research findings are listed as follows:

1) The fast-acting DC breaker (operating time is around 5 ms) does not have any significant impact on the AC/DC system dynamics. Conversely, the severe damage caused by the slow functioning DC breaker can greatly be reduced by increasing the value of the DC reactor.
2) During the post-disturbance transient period, the power flow response of the grid converter with higher loading level is significantly affected. However, the converter loading level does not affect the steady state operation of the MTDC grid.
3) For an equal loading level, the grid converter with a fast-acting DC breaker is affected the most. In other words, the impact of loading level increases with the decrease of the DC breaker operating time.
4) The reconfiguration of a meshed MTDC grid degrades the power flow considerably with a slow-functioning DC breaker (large breaking time).
5) The transient stability of a DC grid is largely affected by the converter deblocking instant.

The future aim of this research is to verify the effectiveness of the proposed method using a real-time hardware in loop system. Moreover, the criteria of deblocking a converter following the DC fault is yet be established, which will be investigated in the future work.

REFERENCES

[1] R. Shah, J. C. Sanchez, R. Preece, and M. Barnes, "Stability and control of mixed AC-DC systems with VSC-HVDC: A review," *IET Generation, Transmission & Distribution*, vol. 12, no. 10, pp. 2207-2219, May 2018.

[2] T. An, G. Tang, and W. Wang, "Research and application on multi-terminal and DC grids based on VSC-HVDC technology in China," *High Voltage*, vol. 2, no. 1, pp. 1–10, 2017.

[3] G. Li, Z. Du, C. Shen, Z. Yuan, and G. Wu, "Coordinated design of droop control in MTDC grid based on model predictive control," *IEEE Trans. Power Syst.,* vol. 33, no. 3, pp. 2816–2828, May 2018.

[4] M. Hassan, R. Shah, and J. Hossain, "Frequency regulation of multiple asynchronous grids using adaptive droop in high-voltage direct current system," *IET Generation, Transmission & Distribution*, vol. 14, no. 7, pp. 1389–1399, Apr. 2020.

[5] X. Li, L. Guo, C. Hong, Y. Zhang, Y. W. Li, and C. Wang, "Hierarchical control of multiterminal dc grids for large-scale renewable energy integration," *IEEE Trans. Sustain. Energy*, vol. 9, no. 3, pp. 1448–1457, Jul. 2018.

[6] N. R. Chaudhuri, R. Majumder, B. Chaudhuri, and J. Pan, "Stability analysis of VSC MTDC grid connected to multi-machine AC systems," *IEEE Trans. Power Del.*, vol. 26, no. 4, pp. 2774-2784, Oct. 2011.

[7] F. Badrkhani Ajaei and R. Iravani, "Dynamic interactions of the MMCHVDC grid and its host AC system due to AC-side disturbances," *IEEE Trans. Power Del*., vol. 31, no. 3, pp. 1289–1298, Jun. 2016.

[8] S. Sanchez, A. Garces, G. Bergna, and E. Tedeschi, "Dynamics and stability of meshed multi-terminal HVDC networks," *IEEE Trans. Power Syst.*, vol. 34, no. 3, pp. 1824-1833, May 2019.

[9] W. Wang, M. Barnes, O. Marjanovic, and O. Cwikowski, "Impact of DC breaker systems on multi-terminal VSC-HVDC stability," *IEEE Trans. Power Del.*, vol. 31, no. 2, pp. 769–779, Apr. 2016.

[10] G. Tang, Z. Xu, and Y. Zhou, "Impacts of three MMC-HVDC configurations on AC system stability under DC line faults," *IEEE Trans. Power Syst*., vol. 29, no. 6, pp. 3030–3040, Nov. 2014.

[11] R. Shah, R. Preece, and M. Barnes, "Impact of MTDC grid reconfiguration and control on the dynamics of the GB system," in *Proc. 15th IET International Conference on AC and DC Transmission*, 2019, pp. 1-6.

[12] D. Zhou, M. H. Rahman, L. Xu, and Y. Wang, "Impact of DC protection strategy of large HVDC network on frequency response of connected AC grid," *The Journal of Engineering*, vol. 2019, no. 17, pp. 4031-4035, Jun. 2019.

[13] A. G. Endegnanew, K. Uhlen, T. M. Haileselassie, and O. Anaya-Lara, "Transient stability analysis in multi-terminal VSC-HVDC grids," in *Proc. Power System Computation Conference*, Jun. 2016, pp. 1–7.

[14] G. O. Kalcon, G. P. Adam, O. Anaya-Lara, S. Lo, and K. Uhlen, "Small-signal stability analysis of multi-terminal VSC-based dc transmission systems," *IEEE Trans. Power Syst.*, vol. 27, no. 4, pp. 1818-1830, Nov. 2012.

[15] W. Du, Q. Fu, and H. Wang, "Small-signal stability of an AC/MTDC power system as affected by open-loop modal coupling between the VSCs," *IEEE Trans. Power Syst.*, vol. 33, no. 3, pp. 3143–3152, May 2018.

[16] A. Bayo-Salas, J. Beerten, J. Rimez, and D. Van Hertem, ''Impedance based stability assessment of parallel VSC HVDC grid connections,'' in *Proc. 11th IET International Conference on AC and DC Transmission*, 2015, pp. 1-9.

[17] H. Zheng, L. Zhou, P. Sun, and W. Lu, "Large-signal stability analysis for VSC-HVDC systems based on mixed potential theory," *IEEE Trans. Power Del.*, vol. 35, no. 4, pp. 1939-1948, Aug. 2020.

[18] A. Sajadi, R. Preece, and J. V. Milanovic, "Evaluation of suitability of different transient stability indices for identification of critical system states", in *Proc. 10th Bulk Power Systems Dynamics and Control Symposium*, 2017, pp. 1-7.

[19] J. Peralta, H. Saad, S. Dennetière, J. Mahseredjian, and S. Nguefeu, "Detailed and averaged models for a 401-level MMC-HVDC system," *IEEE Trans. Power Del.*, vol. 27, no. 3, pp. 1501–1508, Jul. 2012.

[20] O. Anaya-Lara, F. M. Hughes, N. Jenkins, *et al*., "Influence of windfarms on power system dynamic and transient stability," *Wind Energy*, vol. 30, no. 2, pp. 107–127, 2006.

[21] P. M. Anderson, and A. A Fouad, *Power System Control and Stability*, IEEE Press, 1993.

[22] P. Kundur, *Power System Stability and Control*, McGraw-Hill, Inc., 1994.

[23] PowerFactory 2018 SP1 User Manual, "Digsilent gmbh," Gomaringen, Germany, Feb. 2018.

[24] O. D. Adeuyi, M. Cheah-Mane, J. Liang, and N. Jenkins, "Fast frequency response from offshore multi-terminal VSC-HVDC schemes," *IEEE Trans. Power Del*., vol. 32, no. 6, pp. 2442–2452, Dec. 2017.

[25] S. Akkari, J. Dai, M. Petit, and X. Guillaud, "Coupling between the frequency droop and the voltage droop of an AC/DC converter in an MTDC system," in *Proc. IEEE Eindhoven P.Tech*, Jun. 2015, pp. 1–6.

[26] M. Langwasser, G. De Carne, M. Liserre and M. Biskoping, "Fault Current Estimation in Multi-Terminal HVdc Grids Considering MMC Control," *IEEE Trans. Power Syst*., vol. 34, no. 3, pp. 2179-2189, May 2019.

[27] N. A. Belda, C. A. Plet and R. P. P. Smeets, "Analysis of Faults in Multiterminal HVDC Grid for Definition of Test Requirements of HVDC Circuit Breakers," *IEEE Trans. Power Del*., vol. 33, no. 1, pp. 403-411, Feb. 2018.

[28] O. Cwikowski, A. Wood, A. Miller, M. Barnes and R. Shuttleworth, "Operating DC Circuit Breakers With MMC," *IEEE Trans. Power Del*., vol. 33, no. 1, pp. 260-270, Feb. 2018.

[29] J. Descloux et al., "HVDC meshed grid: Control and protection of a multi-terminal HVDC system," *CIGRE Org*., vol. 64, no. 8, pp. 835–838, 2013.

[30] R. Li, L. Xu, and L. Yao, "DC fault detection and location in meshed multi-terminal HVDC systems based on DC reactor voltage change rate," *IEEE Trans. Power Del.*, vol. 32, no. 3, pp. 1516–15126, Jun. 2017.

[31] M. Callavik, A. Blomberg, J. Hafner, and B. Jacobson, "The hybrid HVDC breaker - an innovation breakthrough enabling reliable HVDC grids," *ABB Grid Syst., Tech Rep*., pp. 1–10, Nov. 2012.

[32] W. Lin, D. Jovcic, S. Nguefeu, and H. Saad, "Modelling of high power mechanical DC circuit breaker," in *Proc. IEEE Asia Pacific Power & Energy Eng. Conf.,* Brisbane, QLD, Australia, Nov. 2015, pp. 1–5.

[33] L. Tang and B. Ooi, "Locating and isolating DC faults in multi-terminal DC systems," *IEEE Trans. Power Del.*, vol. 22, no. 3, pp. 1877–1884, Jul. 2007.

[34] A. E. Leon, "Short term frequency regulation and inertia emulation using an MMC based MTDC system," *IEEE Trans. Power Syst.,* vol. 33, no. 3, pp. 2854-2863, Jun. 2018.